Spatiotemporal mapping of mesoscopic liquid dynamics

Zhiqiang Shen [○],[1] Jihong Ma [○],[1,*] Jan-Michael Y. Carrillo [○],[1] Wei-Ren Chen,[2] Bobby G. Sumpter,[1] and Yangyang Wang [○][1,†]

[1]*Center for Nanophase Materials Sciences, Oak Ridge National Laboratory, Oak Ridge, Tennessee 37831, USA*
[2]*Neutron Scattering Division, Oak Ridge National Laboratory, Oak Ridge, Tennessee 37831, USA*

The study of liquid dynamics at mesoscopic scales is still strewn with difficulty due to limitations in theory and experiment. Historically, significant attention has been given to the analysis of space-time correlation functions and their frequency-Fourier transforms at a few discrete wave numbers. The massive computing power afforded by modern high performance computing clusters and the advent of a wide-angle neutron spin-echo spectrometer, however, have unlocked a more intuitive and fruitful approach to this problem. Using molecular dynamics simulations, here we demonstrate the benefits of spatiotemporally mapping intermediate scattering functions on a dense grid of correlation times and wave numbers. Four model systems are investigated: a Lennard-Jones liquid, a coarse-grained bead-spring polymer, a molten sodium chloride, and a poly(ethylene oxide) melt. We show that the spatiotemporal mapping approach is particularly useful for elucidating the mesoscopic dynamics in these liquids, where several underlying mechanisms, such as molecular relaxations, hydrodynamic modes, and nonhydrodynamic excitations, are potentially at play. Compared to the traditional method, direct visualization of density space-time correlation functions on two-dimensional color maps permits appraisals of complicated dynamical behavior at mesoscales in a global manner. For example, the scaling relations between space and time for different types of molecular motions can be straightforwardly identified on these plots, without any model-dependent analysis. Additionally, we show how theoretical ideas regarding collective mesoscopic dynamics, such as the classical hydrodynamic theory, the convolution approximation, and a recently proposed phenomenological model, can be discussed in terms of the global features of spatiotemporal maps of intermediate scattering functions. The new perspective offered by the spatiotemporal mapping method should prove useful for the study of liquid dynamics in general.

I. INTRODUCTION

The dynamics of liquids on mesoscales is a problem of longstanding interest for theorists and experimentalists alike. A focal point of past and ongoing studies on this subject is the understanding of spatial and temporal fluctuations of liquid density, with the help of radiation scattering experiments and computer simulations [1–4]. While extraordinary progress has been made as a result of extensive investigations of more than half a century, many problems remain unresolved. For example, the *collective* mesoscopic dynamics of liquids is still poorly understood: coherent inelastic neutron scattering data in this regime are extremely limited [5–9] and there are currently no universally accepted theory for interpreting experimental results. From a theoretical perspective, it has long been recognized that collective mesoscopic motions are generally governed by complicated physical mechanisms and considerations of both molecular dynamics and hydrodynamics are required [4]. Computationally, the situation is much better: a significant body of molecular dynamics simulation data have been accumulated on collective dynamics of atomic,

molecular, metallic, ionic, and polymeric liquids [10–17]. However, without an effective framework to guide the data analysis, the true value of such simulations may yet be unearthed.

In this work we demonstrate and advocate a more natural way of thinking about mesoscopic liquid dynamics. As is known, intermediate scattering functions [$S(q, t)$ and $S_{\mathrm{inc}}(q, t)$], as well as their spatial and temporal Fourier transforms, are vehicles for characterizing the dynamical behavior of liquids. Mathematically, they are mappings defined on a *two-dimensional* plane of wave numbers q and correlation times t. Due to historical and practical reasons, these time correlation functions are typically determined at a few discrete wave numbers (angles) in scattering experiments or computer simulations—that is to say, only a small number of *one-dimensional* slices of these functions are examined. An alternative approach is to survey the entire two-dimensional surface of the intermediate scattering functions. This is exactly what the present study explores. We will refer to this method as *spatiotemporal mapping*.

Computing time correlation functions from molecular dynamics simulations is generally straightforward. By contrast, as we shall show in this work, frequency (energy) domain analysis from simulations can be highly nontrivial for mesoscopic collective liquid dynamics, because of the complicated and subtle features involved. Experimentally, the advent of

---

*Present address: Department of Mechanical Engineering, University of Vermont, Burlington, Vermont 05405, USA.

†wangy@ornl.gov

a wide-angle neutron spin-echo spectrometer [18] has made it possible to efficiently map out the intermediate scattering function over a large swath of momentum transfers and Fourier times in the mesoscopic region. It is worth mentioning that presenting inelastic scattering results in terms of two-dimensional color maps of momentum and energy transfers has been a popular choice at many neutron and x-ray facilities. Nevertheless, the potential benefits of 2D data analysis have not been fully appreciated by the liquid and soft matter dynamics community. Lastly, the advances in parallel computing technologies can be leveraged to significantly accelerate spatiotemporal mapping of intermediate scattering functions from molecular dynamics simulations, particularly for polymeric materials. These considerations provide the technical motivation of this work.

The spatiotemporal mapping method affords a fruitful paradigm for making new observations with inelastic scattering experiments and computer simulations. For example, we shall show that the scaling relation between space and time for density fluctuations can be directly visualized by examining the two-dimensional surfaces of intermediate scattering functions. We shall also demonstrate how different theories and ideas regarding mesoscopic liquid dynamics can be appraised from a global perspective. This study employs molecular dynamics simulations as the research tool, but the same methodology is also applicable to neutron spin-echo experiments, with some caveats.

II. COMPUTATIONAL METHODS

A. Molecular dynamics simulation

Molecular dynamics simulations were performed with the LAMMPS package [19–21]. To showcase the potential of the spatiotemporal mapping approach in a general manner, we report results on four representative systems: a Lennard-Jones liquid, a coarse-grained bead-spring polymer, a molten sodium chloride, and a poly(ethylene oxide) melt. The velocity-Verlet integration algorithm is adopted for the time integration. Equilibrium molecular dynamics simulations are performed in three different ensembles, NVE, NVT, and NPT, in order to obtain all the thermodynamic properties and transport coefficients of interest. The details of the simulation models and procedures are presented below.

1. Lennard-Jones liquid

The standard Lennard-Jones (LJ) model has been extensively studied by molecular dynamics simulations in the past 60 years or so [10,22–26]. Historically, these simulations have greatly facilitated theoretical understanding of current and density fluctuations at finite wavelengths and frequencies [10,22–24,27–31]. Nevertheless, to the best of our knowledge, the space-time correlation functions of this model system have never been mapped out in a *two-dimensional* (2D) fashion. By revisiting this classical liquid, we wish to show how the spatiotemporal mapping approach provides new perspectives on the dynamics of this supposedly well understood system.

Here we adopt the usual Lennard-Jones liquid model with the 6-12 potential [10,22–24,27,29–34], where the interaction between any two atoms (beads) is described by the

following formula:

$$U_{\mathrm{LJ}}(r) = \begin{cases} 4\epsilon\left[\left(\frac{\sigma}{r}\right)^{12} - \left(\frac{\sigma}{r}\right)^{6}\right] - 4\epsilon\left[\left(\frac{\sigma}{r_c}\right)^{12} - \left(\frac{\sigma}{r_c}\right)^{6}\right], & r < r_c, \\ 0, & r \geqslant r_c, \end{cases}$$

$$(1)$$

with r being the distance between two beads, ϵ the energy unit, and σ the bead diameter. The cut-off distance of r_c is set at 2.5 σ. To ensure that the LJ system is in a fluid state, we consider a bead number density of $\rho = 0.88\ \sigma^{-3}$ and a temperature of $T = 1.0$ [29,35–37]. The entire system consists of 32 000 beads, each with mass m. The time step Δt for the integration is 0.005 τ, with $\tau = \sigma(m/\epsilon)^{1/2}$.

2. Coarse-grained polymer

Much of the analysis in this work centers around a coarse-grained (CG) bead-spring model of polymer melts [38–40]. The nonbonded interaction between beads is described by the LJ potential given in Eq. (1), with the same cutoff distance $r_c = 2.5\ \sigma$ [39]. A finitely extensible nonlinear elastic (FENE) potential coupled with purely repulsive Weeks-Chandler-Andersen (WCA) potential [41] is used to connect two neighboring beads along a polymer chain:

$$U_{\mathrm{FENE}}(r) = -\tfrac{1}{2}kR_0^2\ln[1 - (r/R_0)^2] + U_{\mathrm{WCA}}(r), \quad (2)$$

where $R_0 = 1.5\ \sigma$ and $k = 30\ \epsilon/\sigma^2$. Additionally, a bond-bending potential is considered:

$$U_{\mathrm{bend}}(\theta) = k_\theta(1 + \cos\theta), \quad (3)$$

where θ is the angle between two subsequent bonds and $k_\theta = 0.75\ \epsilon$ [40]. Each chain has N beads of mass m. For both the LJ liquid and the CG polymer simulations, LJ units are used to present the simulation results by setting $\sigma = \epsilon = m = 1$ and the Boltzmann constant $k_{\mathrm{B}} = 1$.

To systematically investigate the effect of temperature on the mesoscopic dynamics of polymers, we considered an unentangled melt consisting of $M = 8000$ chains, each with $N = 25$ repeating units. Seven different temperatures were investigated: $T = 1.0, 0.9, 0.8, 0.7, 0.6, 0.5,$ and 0.48. The number density of beads was kept at a constant $\rho = 1.0\ \sigma^{-3}$. As is the case with all the other simulations in this work, equilibrium molecular dynamics simulations were carried out in three different ensembles, i.e., NVE, NVT, and NPT, in order to obtain all the relevant thermodynamic properties and transport coefficients. To guarantee a fully equilibrated state for the production run, the system was first relaxed under NVT condition for more than 5000 τ_α at each temperature, where τ_α is the α relaxation time. The time step Δt for integration in the CG polymer simulation was 0.01 τ.

3. Sodium chloride melt

To further explore the mesoscopic dynamics with the spatiotemporal mapping approach, we considered a rigid-ion atomistic model for sodium chloride (NaCl) melt. Specifically, the interaction between any two ions i and j in the system is described by the Mayer-Huggins-Tosi-Fumi potential of the form [42–44]

$$U(r) = A_{ij}\exp\left(\frac{\sigma_i + \sigma_j - r}{\rho_{\mathrm{MH}}}\right) - \frac{C_{ij}}{r^6} + \frac{D_{ij}}{r^8} - \frac{z_iz_j}{r}, \quad (4)$$

where σ_i and σ_j are the basic radii of the ions i and j, ρ_{MH} is the characteristic "hardness parameter," and z_i and z_j are the ionic charges. All the potential coefficients in our simulations follow those in Ref. [42]. The cutoff distance for the non-Coulombic interaction is 10 Å.

In our simulation, 5000 pairs of Na and Cl ions were initially randomly placed in a box of $80 \times 80 \times 80$ Å^3. To ensure an equilibrium state before the production run, the system was first relaxed at a high temperature of 1600 K with a constant volume for 200 ps. Its pressure was then gradually decreased to zero through the Nosé-Hoover barostat. Afterwards, the ionic melt was cooled down to $T = 1480$ K within 100 ps and further relaxed under zero pressure for 1 ns. This fully equilibrated system served as the initial configuration for molecular dynamics simulations in NVE, NVT, and NPT ensembles. The step used in the time integration was 1 fs. The long-range Coulombic interaction was calculated using the particle-particle particle-mesh (PPPM) solver [45] with a force tolerance of 10^{-5}.

4. Poly(ethylene oxide) melt

Finally, we present results of atomistic simulations on a representative polymer melt: poly(ethylene oxide) (PEO). The chosen model of PEO was based on the General Amber Force Field (GAFF) [46] with optimized coefficients for both intra- and intermolecular potentials. Specifically, the potential coefficients were improved by comparing the force field predictions for various conformations of 1,2-dimethoxyethane [47] with density functional theory calculations performed at B3LYP/6-31G* level with the NWChem software [48]. The details of the force field are described in the Appendix.

This work focuses on an unentangled PEO melt with 64 chains, each containing 48 repeating units. The chains were initially put in a simulation box at low density and relaxed at 600 K and constant volume for 600 ps through the Nosé-Hoover thermostat. Subsequently, the temperature was gradually decreased to the target temperature of 363 K. At the same time, the pressure of the system was ramped down to 1 atm through the Nosé-Hoover barostat. The duration of this relaxation process was approximately 1 ns. Afterwards, further equilibration was carried out at the same temperature (363 K) and pressure (1 atm) for 16 ns. The fully relaxed system was used as the initial configuration in the subsequent equilibrium molecular dynamics simulations for NVE, NVT, and NPT ensembles. The time step for the integration was 1 fs.

B. Spatiotemporal mapping

In this work, the (normalized) coherent and incoherent intermediate scattering functions of the aforementioned systems are computed on a dense grid of correlation times and wave numbers, and the results are presented in the form of two-dimensional color maps (heat maps). To discuss both the coarse-grained and atomic models in a unified way, the following definition of the coherent intermediate scattering function (before normalization) is adopted:

$$S(\mathbf{q}, t) = \frac{1}{N} \sum_{i,j}^{N} \langle b_i b_j \exp[i\mathbf{q} \cdot (\mathbf{r}_j(t) - \mathbf{r}_i(0))] \rangle, \quad (5)$$

where N is the total number of beads or atoms, and b_i is the coherent scattering length. For the two coarse-grained models, b_i equals unity. For the NaCl melt, $b_{Na} = 3.63$ fm and $b_{Cl} = 9.577$ fm. On the other hand, we consider the PEO melt as *fully deuterated*, for calculations of both coherent and incoherent scattering functions. We have $b_c = 6.6511$ fm, $b_D = 6.67$ fm, and $b_O = 5.803$ fm [49,50]. $\mathbf{r}_i(t)$ is the position of the ith atom or bead at time t. $\mathbf{q}$ are wave vectors that commensurate with the periodical condition in simulations, i.e., $\mathbf{q} = (2\pi/L)(n_x, n_y, n_z)$, where n_x, n_y, n_z are integers and L is the length of the simulation box [3]. Similarly, the incoherent intermediate scattering function is defined as

$$S_{inc}(\mathbf{q}, t) = \frac{1}{N} \sum_{j=1}^{N} \langle b_{inc,j}^2 \exp[i\mathbf{q} \cdot (\mathbf{r}_j(t) - \mathbf{r}_j(0))] \rangle, \quad (6)$$

where $b_{inc,j}$ is the incoherent scattering length for the jth atom or bead. b_{inc} is unity for the LJ liquid and CG polymer systems. For the NaCl melt, $b_{inc}^{Na} = 3.59$ fm and $b_{inc}^{Cl} = 6.4943$ fm. For the PEO melt, $b_{inc}^c = b_{inc}^O = 0$, and $b_{inc}^D = 4.04$ fm [49]. Since all the systems under investigation are isotropic liquids in the equilibrium state, the reciprocal-space structure does not depend on the orientation of $\mathbf{q}$ and the results are discussed in terms of $S(q, t)$ and $S_{inc}(q, t)$. In this work, both the coherent and incoherent intermediate scattering functions are calculated in the NVT ensemble for all the systems.

Instead of analyzing one-dimensional slices of intermediate scattering functions at a few discrete q values, the dynamic landscape is systematically mapped out and visualized over a large swath of correlation times and wave numbers. This seemingly simple extension of the traditional method turns out to be a highly productive approach. From a technical point of view, such calculations are well suited for parallel computing. The data analysis code in this investigation is optimized for the computational architecture of the Summit supercomputer at the Oak Ridge National Laboratory, through a hybrid framework that utilizes both the message passing interface (MPI) and OpenACC [51].

C. Classical hydrodynamic theory

To get a general concept of how the hydrodynamic interactions play a role in the collective dynamics of liquids and polymers, we need to investigate the hydrodynamic modes in theory. According to the classical theory, the normalized intermediate scattering function $S(q, t)/S(q)$ of the density fluctuations is described by the following equation [4,52–54]:

$$\frac{S(q,t)}{S(q)} = \frac{\gamma - 1}{\gamma} e^{-\chi q^2 t} + \frac{1}{\gamma} e^{-\Gamma q^2 t} \cos(cqt) + \frac{1}{\gamma} \frac{q}{c} [\Gamma + (\gamma - 1)\chi] e^{-\Gamma q^2 t} \sin(cqt), \quad (7)$$

where γ is the specific heat ratio, χ is the thermal diffusivity, c is the adiabatic sound velocity, and Γ is the acoustic attenuation coefficient. The first term on the right-hand side of Eq. (7) comes from the Fourier transform of the Rayleigh central line, whereas the second and third terms are associated with the Brillouin doublet.

It is generally expected that the classical hydrodynamic theory cannot fully describe the density fluctuations at mesoscales, where nonhydrodynamic modes likely play an important role as well. However, the transition from continuum to molecular behavior should occur smoothly, making it difficult to pinpoint any prominent dynamical features for constructing a successful theory. As we shall show in Sec. III, the global perspective offered by the spatiotemporal mapping method can be instrumental in further development of this field. On the other hand, it is not the intention of this work to critically examine various theoretical approaches for treating current and density fluctuations in the "molecular hydrodynamic" regime [4]. Nor can such a task be accomplished without a herculean effort. Our goal here is to illustrate the essential idea of analyzing mesoscopic dynamics from MD simulations by comparing the results with simple models. A full critique of all the major theories will be deferred to future investigations.

To predict the normalized coherent intermediate scattering function $S(q,t)/S(q)$ with the classical hydrodynamic theory [Eq. (7)], four parameters are required: γ, χ, c, and Γ. Methods for evaluating these coefficients from MD simulations have been well established in the literature [3,22,24]. Nevertheless, we briefly describe such procedures below, for the convenience of the readers. First, to compute the specific heat ratio $\gamma = c_p/c_v$, molecular dynamics simulations are performed in two different ensembles: NVT and NPT. The specific heat at constant volume c_v can be estimated from the NVT simulation as $\langle \delta H^2 \rangle_{\mathrm{NVT}} = Nk_{\mathrm{B}}T^2 c_v$, whereas the specific heat at constant pressure c_p can be calculated from the NPT simulation as $\langle \delta(H+PV)^2 \rangle_{\mathrm{NPT}} = Nk_B T^2 c_p$. Here H is the total energy, N is the total number of beads or atoms, and V is the volume of the system. Second, the thermal diffusivity χ is related to the thermal conductivity κ as $\chi = \kappa/(\rho c_p/m)$, ρ is number density and m is the averaged mass per bead or atom in the simulation box. The thermal conductivity can be evaluated from the autocorrelation function of the energy current j_α^ϵ in the NVE simulation by using the Green-Kubo formula [55,56]:

$$\kappa = \frac{V}{k_{\mathrm{B}} T^2} \int_0^\infty \left\langle j_\alpha^\epsilon(t) j_\alpha^\epsilon(0) \right\rangle dt. \tag{8}$$

Third, the adiabatic sound velocity can be computed from the specific heat ratio γ and the isothermal compressibility χ_T as $c = \sqrt{\gamma/(\rho m \chi_T)}$. And χ_T can be derived from the zero-angle scattering as $\chi_{\mathrm{T}} = \lim_{q \to 0} S(q)/(\rho k_{\mathrm{B}} T)$, where $S(q)$ is defined by the particle number density ($b_i = 1$). Lastly, to obtain the acoustic attenuation coefficient Γ, the information about longitudinal viscosity η_L is needed: $\Gamma = \frac{1}{2}[(\eta_L/\rho + (\gamma - 1)\chi]$. Once again, one can employ the Green-Kubo relation [3]:

$$\eta_L = \frac{V}{k_{\mathrm{B}} T} \int_0^\infty \langle \delta P_{\alpha\alpha}(t) \delta P_{\alpha\alpha}(0) \rangle \, dt. \tag{9}$$

Here $\delta P_{\alpha\alpha}$ is the fluctuation of the diagonal component of the pressure tensor in the NVE simulation: $\delta P_{\alpha\alpha}(t) = P_{\alpha\alpha}(t) - \langle P_{\alpha\alpha} \rangle$, with $\alpha = x, y$, or z.

III. RESULTS AND DISCUSSION

The discussion of simulation results is divided into three sections. We first analyze in detail the behavior of the coarse-grained polymer melt through the lens of spatiotemporal maps of intermediate scattering functions. Specifically, we discuss the results in light of the classical hydrodynamic theory, the convolution approximation idea of Vineyard, de Gennes, and Sköld [57–60], and a recently proposed phenomenological model for mesoscopic collective liquid dynamics by Novikov *et al.* [61]. Our intention is *not* to present a systematic critique of the existing experiments, simulations, theories, and models regarding mesoscopic liquid dynamics. Instead, the primary goal of this work is to illustrate the usefulness of the spatiotemporal mapping method with clear and simple examples. In Sec. III B we discuss the similarities and differences between the two coarse-grained systems: the bead-spring polymer melt and the Lennard-Jones liquid. Finally, Sec. III C shows the application of the spatiotemporal mapping analysis to more "realistic" systems by presenting the results on atomistic models of sodium chloride and poly(ethylene oxide).

A. Coarse-grained polymer

Some of the basic structural, thermodynamic, transport properties of the coarse-grained polymer melt are shown in Fig. 1. Additionally, tabulated data for all the simulated liquids: the Lennard-Jones liquid, coarse-grained bead-spring polymer, molten sodium chloride, and poly(ethylene oxide) melt are reported in Table I. As indicated in Sec. II, these simulations probe the behavior of the polymer melt at various temperatures with fixed number density (isochoric condition). The static structure factor $S(q)$ is given in Fig. 1(a). Consistent with reports in the literature, the first structural peak is observed around $q_{\max} \simeq 7.1 \ \sigma^{-1}$ and the peak height slightly increases with decrease of temperature [62]. The static structure factor is flat in the low q region, and the zero-angle scattering amplitude at each temperature $S(0) \equiv \lim_{q \to 0} S(q)$ is obtained by fitting $S(q)$ at small q ($q < 1 \ \sigma^{-1}$) to a horizontal line. As shown in Fig. 1(b), $S(0)$ increases from 0.017 at $T = 0.48$ to 0.023 at $T = 1.0$, implying a relatively weak temperature dependence of isothermal compressibility within the tested temperature range χ_T (please also see Table I). The specific heats at constant volume and constant pressure c_v and c_p are presented in Figs. 1(c) and 1(d), and both of them decrease with increase of temperature. On the other hand, the longitudinal viscosity η_L and thermal conductivity κ become slightly larger as the temperature is raised [Figs. 1(e) and 1(f)]. Because the particle number density is fixed in these simulations, the equilibrium pressure drops considerably at low temperatures. This helps to explain the somewhat counterintuitive decrease of longitudinal viscosity with decrease of temperature. Overall, these thermodynamic and transport coefficients of the CG polymer melt do not change significantly over the examined temperature range.

TABLE I. Basic properties of different systems: zero-angle scattering $S(0) \equiv \lim_{q \to 0} S(q)$, longitudinal viscosity η_L, thermal conductivity κ, specific heat at constant pressure c_p, specific heat at constant volume c_v, specific heat ratio γ, thermal diffusivity χ, acoustic attenuation coefficient Γ, and adiabatic sound velocity c. For both the LJ liquid and CG polymer, the reduced LJ units are used. For the NaCl and PEO melt, the units of η_L, κ, and $c_p(c_v)$ in the table are mPa s, W/(mK), and, J/(mol K), respectively. c_p and c_v are normalized by the corresponding total number of Na and Cl ions pairs and PEO repeating units. Additionally, χ, Γ, c are expressed with the units of Å^2/ps, Å^2/ps, and Å/ps, respectively. Monoatomic assumption is used for NaCl and PEO to obtain the zero-angle scattering $S(0)$ for the hydrodynamic theory.

Systems	$S(0)$	η_L	κ	c_p	c_v	γ	χ	Γ	c
LJ liquid	0.0351	6.277	8.434	4.385	2.612	1.68	2.19	4.31	6.91
NaCl melt	0.1986	2.400	0.500	69.93	51.75	1.35	30.5	93.0	14.9
PEO melt	0.3067	0.794	1.226	215.2	193.9	1.11	23.8	39.0	13.2
CG polymer, $T = 1.0$	0.0232	6.673	8.759	4.201	3.039	1.38	2.08	3.73	7.71
CG polymer, $T = 0.9$	0.0220	6.619	8.700	4.306	3.094	1.39	2.04	3.70	7.51
CG polymer, $T = 0.8$	0.0208	6.632	8.326	4.307	3.167	1.36	1.86	3.70	7.36
CG polymer, $T = 0.7$	0.0202	6.577	8.220	4.565	3.280	1.39	1.79	3.65	6.97
CG polymer, $T = 0.6$	0.0191	6.570	8.014	4.873	3.377	1.44	1.67	3.63	6.67
CG polymer, $T = 0.5$	0.0177	6.581	7.990	5.064	3.500	1.45	1.63	3.61	6.27
CG polymer, $T = 0.48$	0.0172	6.526	7.942	5.281	3.518	1.50	1.58	3.60	6.32

1. Collective dynamics and hydrodynamic modes

The spatiotemporal maps of the normalized coherent intermediate scattering function $S(q,t)/S(q)$ of the coarse-grained polymer melt are shown in Fig. 2(a), with the magnitude of $S(q,t)/S(q)$ described by the "jet" color scheme [63]. The
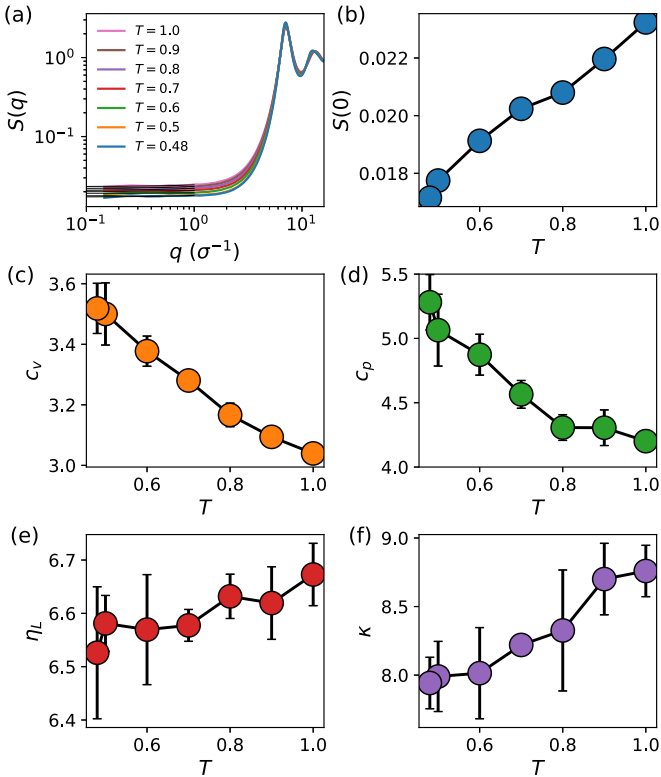

FIG. 1. Basic properties of the coarse-grained polymer melt at various temperatures: (a) static structure factor $S(q)$, (b) zero-angle scattering $S(0) \equiv \lim_{q \to 0} S(q)$, (c) specific heat at constant volume c_v, (d) specific heat at constant pressure c_p, (e) longitudinal viscosity η_L, and (f) thermal conductivity κ. Black horizontal lines in (a): fitting used to extract $S(0)$. The reported data are based on five independent simulations.

reddish part of the spectrum implies strong correlation, i.e., $S(q,t)/S(q) \approx 1$, whereas the blue color indicates loss of correlation, i.e., $S(q,t)/S(q) \approx 0$. Generally speaking, two slowly relaxing regions are observed in the 2D map of the coarse-grained polymer. One is located around the first structural peak $q_{max} \simeq 7.1 \ \sigma^{-1}$, which is widely known as the de Gennes narrowing [57,64–67]. This phenomenon is commonly attributed to collective motions of atoms to escape their preferred structural positions. The characteristic relaxation time of $S(q,t)/S(q)$ at q_{max} increases dramatically as the temperature is lowered. Beyond the first peak, another slowly relaxing region is found at $q < 1 \ \sigma^{-1}$, which is approximately ten times smaller than q_{max} and usually called mesoscale or intermediate q range.

An immediate benefit of presenting the intermediate scattering function as a two-dimensional color map is that the intrinsic relation between space and time for a certain type of molecular motion can be directly revealed by analyzing the slope of the contour lines. Interestingly, for the mesoscopic dynamics featured on the bottom left corners of these plots, the decay of intermediate scattering function is underpinned by an inverse relation between wave number and correlation time [Fig. 2(a)], with a characteristic slope of -1 on the 2D map. It is easy to verify that contour lines of a normal Fickian diffusion exhibit a slope of $-1/2$ on such a map, whereas any sub-diffusive behavior leads to a (negative) slope of smaller magnitude.

What does the slope of -1 imply? Recall that according to the classical hydrodynamic theory, the characteristic frequency shift associated with the Brillouin doublet is proportional to the scattering wave number: $\Delta\omega \propto q$. Analyzing this directly in the time domain, we see from Eq. (7) that the thermal diffusivity mode (first term) should produce contour lines with a slope of $-1/2$ on the 2D map; the sine and cosine functions in the Brillouin doublet terms, on the other hand, should give rise to a characteristic slope of -1; additionally, these spatiotemporal oscillations should be further modulated by acoustic attenuation, which is a normal diffusive process with a slope of $-1/2$. Using the thermodynamic and transport coefficients obtained from the equilibrium molecular
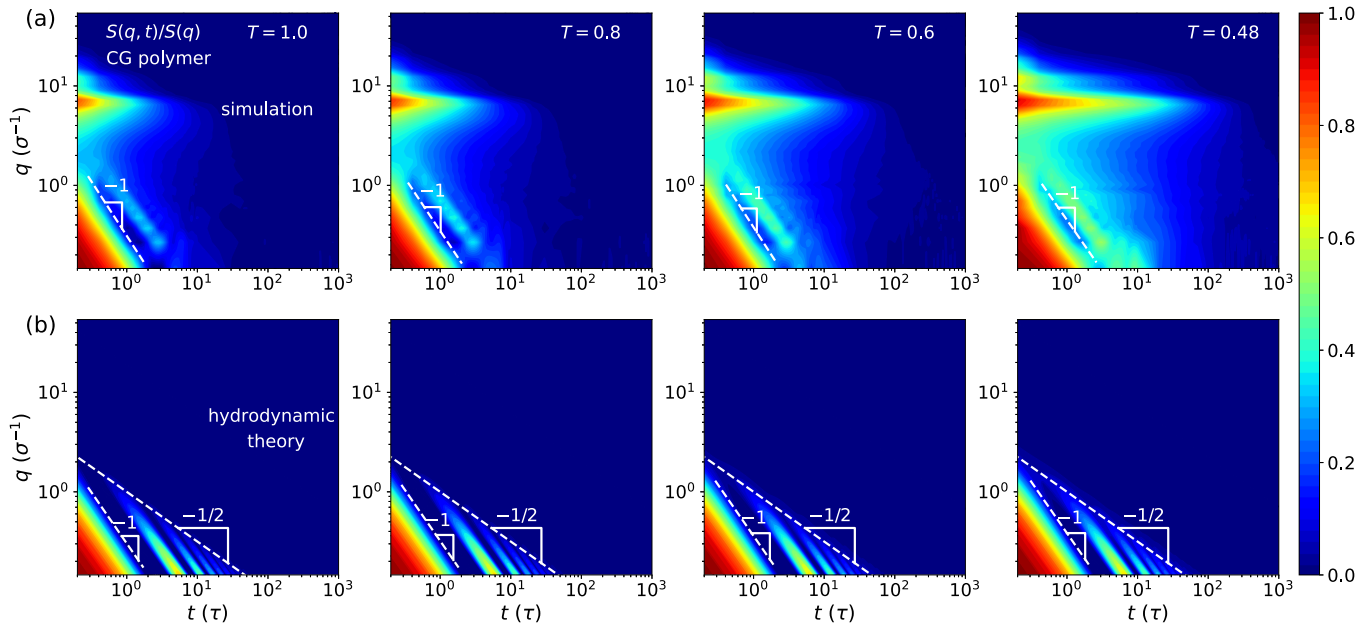
FIG. 2. Spatiotemporal mapping of normalized coherent intermediate scattering function of the coarse-grained polymer melt. (a) 2D maps of $S(q,t)/S(q)$ obtained from the simulations at various temperatures. (b) Corresponding predictions by the classical hydrodynamic theory. The white dashed lines indicate the characteristic slope for the hydrodynamic modes.

dynamics simulations, we can visualize the predictions of the classical hydrodynamic theory for the coarse-grained polymer melt on a spatiotemporal map as well. The results of these calculations are presented in Fig. 2(b).

As expected, the Brillouin doublet reveal themselves as sinusoidal oscillations on the spatiotemporal map, with a characteristic slope of -1. Furthermore, they are enveloped by a diffusive mode with a slope of $-1/2$. Evidently, the classical hydrodynamic theory is able to capture the major decay of the intermediate scattering function on the mesoscopic scale in a nearly quantitative manner. However, the predicted "higher order" oscillations at long correlation times are not observed in the molecular dynamics simulations, suggesting a stronger attenuation effect that is not considered by the theory. In addition, while the theory is able to depict the location of the "second ridge" of oscillation beyond the first decay, the theory and simulation do not agree on details. The simulation not only shows a stronger damping at low wave number and long correlation time, but also produces small peaks that are not foreseen by the theory. Lastly, as the temperature is lowered, higher correlation of density fluctuation is found in the molecular hydrodynamic regime. This phenomenon is likely to stem from a coupling between structural relaxation and hydrodynamic modes. We note that many of the subtle features discussed here cannot be easily identified without a systematic mapping of the normalized coherent intermediate scattering function—the traditional one-dimensional data analysis approach would fall short in comparison.

The dynamics of liquids at mesoscopic scale is known to have a complicated molecular origin. Although the concept of molecular hydrodynamics has long been recognized [4], the transition from molecular dynamics to hydrodynamics is also expected to be smooth. Moreover, most of the theoretical studies focus on relatively simple liquids, whereas interesting systems in the real world are mostly complex fluids that

require further careful consideration. Even if we wish to answer the simplest question—where do hydrodynamic modes matter—this generally cannot be done without doing some serious calculations. In this regard, the spatiotemporal mapping approach demonstrated here is of vital importance: to obtain a lucid understanding of molecular motions on mesoscale, we need to first systematically map out the dynamic landscape.

2. Self-dynamics and convolution approximation

Having examined the collective dynamics of the coarse-grained polymer melt, we now turn our attention to the spatiotemporal map of the incoherent intermediate scattering function $S_{\text{inc}}(q,t)$ [Fig. 3(a)]. In the region of small t and large q, the slope of the contour lines is found to be -1, which corresponds to the ballistic motions of atoms. The slope of the contour lines decreases beyond this free-motion regime and enters into a region with a slope of $-1/4$ at high temperature (e.g., $T = 1.0$). This scaling of $-1/4$ is associated with the well-known Rouse dynamics [68]: $S_{\text{inc}}(\tilde{q}, \tilde{t}) = \exp(-\frac{2}{\pi^{3/2}}\tilde{q}^2\tilde{t}^{1/2})$, where $\tilde{q} = qR_{\text{G}}$ and $\tilde{t} = t/\tau_{\text{R}}$. Here R_{G} is the radius of gyration of the polymer chain and τ_{R} is the Rouse relaxation time. It is worth noting that the traditional Rouse scaling analysis is accomplished by plotting $S(q,t)/S(q)$ against the reduced variable $q^2t^{1/2}$ [69]. By contrast, the spatiotemporal mapping method permits direct visualizing of scaling relations without the requirement of presenting data in an ad hoc manner. At lower temperatures ($T = 0.6$ and $T = 0.48$), the Rouse regime is eroded by an additional subdiffusive behavior on the intermediate time and length scales, which arises from the so-called cage effect in supercooled liquids [70,71].

To further demonstrate the usefulness of the spatiotemporal mapping approach, we now turn to a widely used phenomenological model known as the Vineyard–de Gennes–
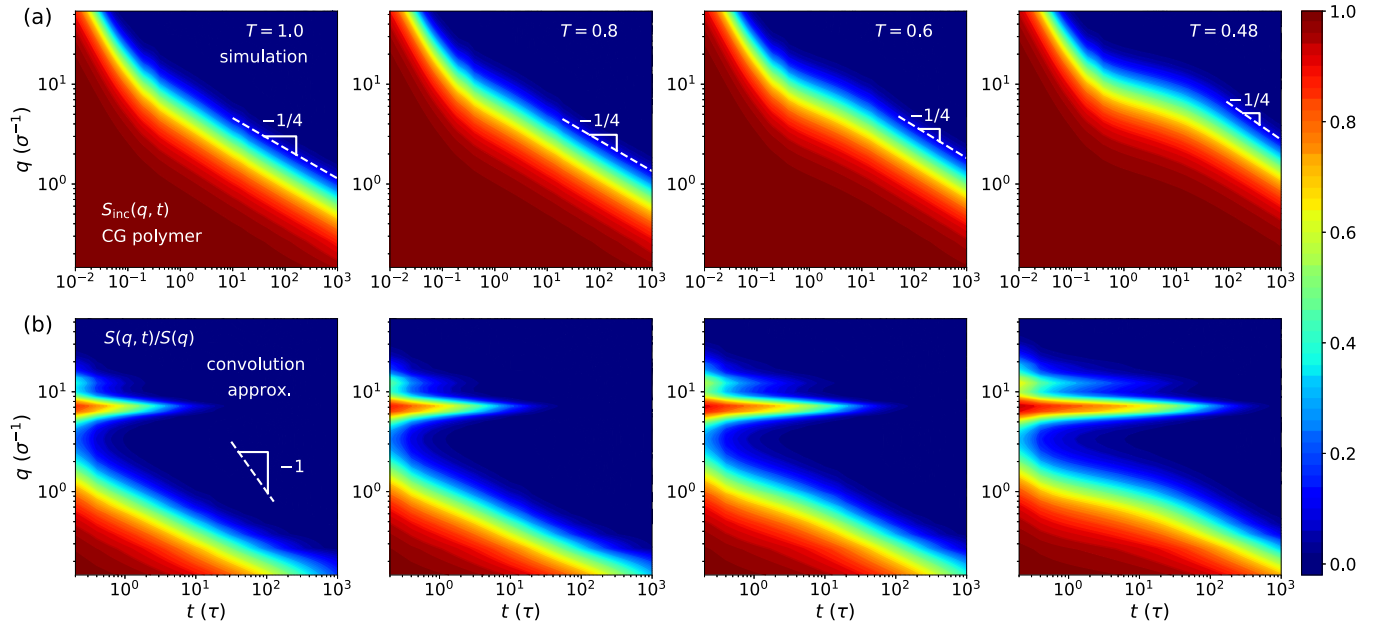
FIG. 3. (a) Spatiotemporal mapping of incoherent intermediate scattering function $S_{\mathrm{inc}}(q,t)$ of the coarse-grained polymer melt at various temperatures. (b) Normalized coherent intermediate scattering function $S(q,t)/S(q)$ generated by the convolution approximation. Note that hydrodynamic modes produce a characteristic slope of -1, which is not observed in (b).

Sköld convolution approximation [57–60], which relates the collective and self-dynamics:

$$S(q,t)/S(q) \approx S_{\mathrm{inc}}[q/\sqrt{S(q)}, t]. \qquad (10)$$

With the two-dimensional maps of $S(q,t)/S(q)$ and $S_{\mathrm{inc}}(q,t)$ at hand [Figs. 2(a) and 3(a)], the merits and shortcomings of the convolution approximation can be evaluated in a global and comprehensive way. Figure 3(b) shows the predictions of the convolution approximation for the normalized intermediate scattering function $S(q,t)/S(q)$. These 2D plots are obtained by performing a mapping of $q \rightarrow q/\sqrt{S(q)}$ for the incoherent intermediate scattering function $S_{\mathrm{inc}}(q,t)$ from the simulation. Comparing these theoretical predictions with the $S(q,t)/S(q)$ 2D maps from simulations [Fig. 2(a)], we see that Eq. (10) only gives a qualitatively reasonable estimation in the high q region. On the other hand, the convolution approximation completely breaks down in the mesoscopic regime beyond the first structural peak, producing qualitatively incorrect behavior. Indeed, this failure itself has long been recognized [4,6]. Nevertheless, the spatiotemporal mapping approach allows one to better appreciate *how* the approximation fails. We further note that the major features of the mesoscopic collective dynamics in Fig. 2(a) do not change significantly within the probed temperature range, whereas the convolution approximation paints an entirely different picture.

3. Application to a phenomenological model

As another illustration of the power of the spatiotemporal mapping analysis, we shall examine in this subsection a recently proposed phenomenological model by Novikov, Schweizer, and Sokolov [61] for mesoscopic collective dynamics. This model has been applied to neutron spin-echo data on sodium potassium nitrate (CKN) [5,61] and an extension of it to polyisobutylene [72,73] in the intermediate

q range. The model claims that the q-dependent relaxation rate of the normalized intermediate scattering function $S(q,t)/S(q)$ can be approximated by the following formula [61]:

$$\frac{1}{\tau(q)} = \frac{1}{\tau_\alpha(0)}e^{-q^2\xi_c^2} + \frac{q^2D}{S(q)+q^2\xi_D^2}. \qquad (11)$$

The first term in Eq. (11) represents the contribution from a q-dependent, nondiffusive structural relaxation (α relaxation): $\tau_\alpha(0)$ is the α relaxation time in the zero-angle limit; $\exp(-q^2\xi_c^2)$ is a Gaussian cutoff factor which ensures that the α relaxation term is only operative beyond a characteristic length of $\xi_c \approx 2\pi/q_{\max}$. The second term in Eq. (11) approximates the relaxation rate on the molecular scale in the high q region, by employing the convolution approximation [Eq. (10)] and the jump diffusion model [74]. Here D is a diffusion constant and ξ_D is a characteristic length scale. To evaluate D and ξ_D, the incoherent scattering function $S_{\mathrm{inc}}(q,t)$ from simulation is fitted by the jump diffusion model as $S_{\mathrm{inc}}(q,t) = A(q)\exp[-\Gamma(q)t]$, where $A(q)$ is the Debye-Waller factor and $\Gamma(q) = Dq^2/[1+(q\xi_D)^2]$ is the relaxation rate. The second term in Eq. (11) is obtained by performing a mapping $q \rightarrow q/\sqrt{S(q)}$ for the relaxation rate $\Gamma(q)$. We note that the original form of the jump-diffusion term in Ref. [61] is not fully consistent with the convolution approximation. The corrected formula [Eq. (11)] is used in our calculation, although this minor difference does not affect the result in any substantial way.

Figure 4 compares the normalized coherent intermediate scattering function from the molecular dynamics simulation with that predicted by Eq. (11) at $T = 0.48$. The theoretical q-dependent relaxation time $\tau(q)$ is shown as dashed lines in Fig. 4(a). Additionally, using the $\tau(q)$ from Eq. (11), the theoretical spatiotemporal map can be computed as $S(q,t)/S(q) \approx$
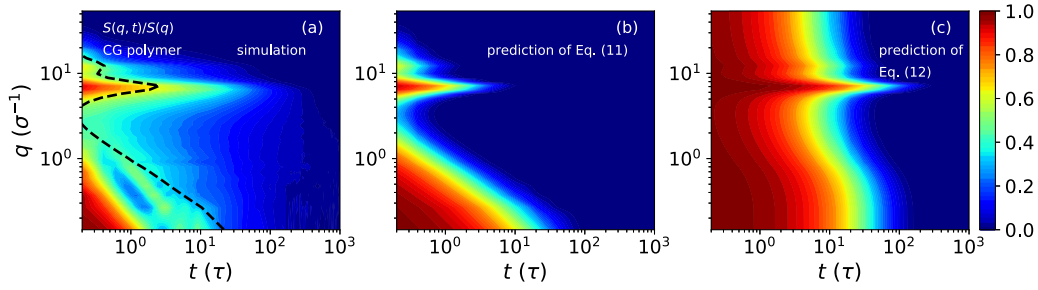
FIG. 4. Comparison between (a) the normalized coherent intermediate scattering function $S(q, t)/S(q)$ from simulation and those obtained from (b) Eq. (11) and (c) Eq. (12). The theoretical $S(q, t)/S(q)$ is computed as $S(q, t)/S(q) = \exp[-t/\tau(q)]$. The black dashed line in (a) indicates the relaxation time $\tau(q)$ given by Eq. (11). The stretching exponent β for Eq. (12) is 0.59.

$\exp[-t/\tau(q)]$ [Fig. 4(b)]. It is helpful to keep in mind that when the intermediate scattering function decays to $\sim \exp(-1) \approx 0.37$ of $S(q)$, the corresponding color on the 2D map should be cyan. Evidently, Eq. (11) is only able to give a qualitatively reasonable estimation in the de Gennes narrowing region at q_{max}, which is hardly surprising given the general success of the convolution approximation at high q. On the other hand, poor agreement is found between the model and simulation in the mesoscopic regime. Additionally, this qualitative failure of the model is insensitive to the choice of ξ_c: no physically reasonable values of ξ_c can produce the correct behavior for $S(q, t)/S(q)$. This analysis shows that the spatiotemporal mapping method translates the abstract mathematical formula [Eq. (11)] into a more tangible object, from which the strengths and weaknesses of the model can be better appraised.

A simple extension of Eq. (11) has been proposed by Colmenero and co-workers [72,73,75] to account for stretched-exponential relaxation. The original equation [72,73] given by Colmenero *et al.* was in fact inconsistent with the convolution approximation, and this issue was addressed by their recent publication [75]. The correct equation reads

$$\frac{1}{\tau(q)} = \frac{1}{\tau_\alpha(0)} e^{-q^2 \xi_c^2} + \frac{D}{\xi_D^2} \left(1 + \frac{S(q)}{q^2 \xi_D^2} \right)^{-\frac{1}{\beta}}, \quad (12)$$

where β is the stretching exponent, and D and ξ_D are obtained by fitting the corresponding stretched-exponential function. To determine β for the CG polymer at $T = 0.48$, the incoherent scattering function $S_{inc}(q, t)$ is fitted by the stretched-exponential function at q values close to q_{max}, yielding a best fit of $\beta = 0.59$. Using this exponent, we produce the prediction of Eq. (12) for $S(q, t)/S(q)$ in Fig. 4(c). Interestingly, the revision proposed by Colmenero *et al.* does not improve the prediction of the model for the CG polymer system in any substantial way. In fact, it results in poorer performance in the high-q region. We emphasize that the analysis presented here should *not* be construed as a direct critique of the model of Novikov and co-workers. First, the model was apparently motivated by the experimental data on CKN [5], which were obtained and analyzed in the traditional way: the intermediate scattering function was determined at a few discrete wave numbers and the relaxation time was extracted via fitting by stretched-exponential functions. Given the complicated behavior of collective mesoscopic dynamics revealed by simulations, it is not obvious if the reported q-dependent

relaxation times should be taken at their face value. Second, it is well known that CKN displays intermediate-range order, as reflected in a "prepeak" in the static structure factor $S(q)$ [76–78]. This undoubtedly further complicates the mesoscopic collective dynamics. None of the systems simulated in this work exhibits intermediate-range order. It remains to be seen whether the reported nonmonotonic q dependence of relaxation is robust and if it is a consequence of intermediate-range order. To faithfully incorporate all the essential physics for mesoscopic dynamics in a simulation model for CKN is not a trivial matter. We therefore defer the analysis of CKN to a future publication, for the reasons stated above. It is helpful to point out that the model of Novikov *et al.* is intended for length scales above intermolecular distances and yet below the "long wavelength hydrodynamic limit." However, our simulations show that hydrodynamiclike modes are operative almost immediately beyond the first structural peak. In this regard, the model of Novikov *et al.* does seem to miss an important theoretical ingredient for the spatiotemporal region of current interest.

B. Lennard-Jones liquid

The preceding discussions demonstrate that the spatiotemporal mapping approach affords a convenient and powerful platform to study the mesoscopic dynamics of the coarse-grained polymer melt. In the following sections we will provide additional examples to show that it indeed can serve as a general method to investigate the dynamics of different fluids. The systems reported here include a Lennard-Jones liquid, an ionic liquid (NaCl melt), and an atomistic polymer model (PEO melt). In each example, we will investigate its collective dynamics by comparing 2D maps of $S(q, t)/S(q)$ generated by simulation and hydrodynamic theory. Additionally, the self-dynamics and the corresponding convolution approximation will also be discussed with the aid of spatiotemporal maps.

As noted in Sec. II, the standard Lennard-Jones model is a classical system that has been widely studied. For historical reasons, most of the investigations were conducted in an era when direct visualization of space-time correlation functions on two-dimensional color maps was generally difficult or even impossible. Here we show that in such a thoroughly plowed field the spatiotemporal mapping approach can still offer new insight into the mesoscopic dynamics.
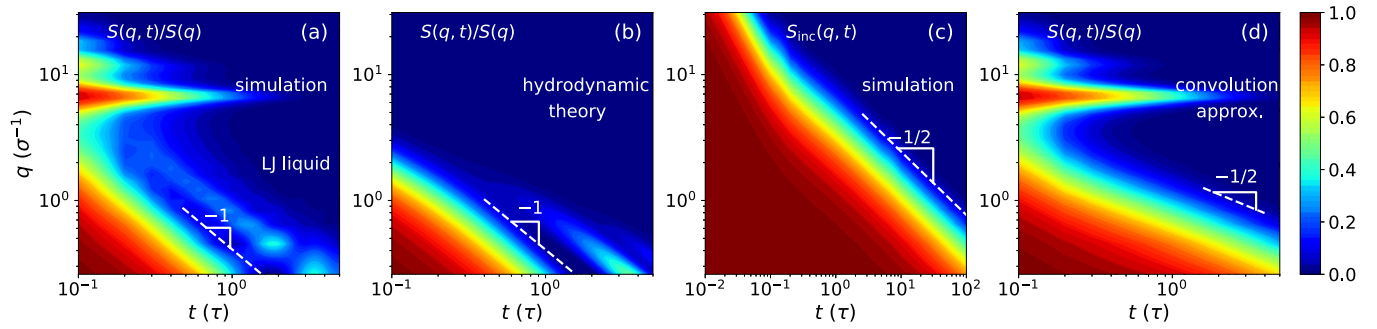
FIG. 5. Spatiotemporal mapping of the intermediate scattering functions of the Lennard-Jones (LJ) liquid at $\rho = 0.88 \, \sigma^{-3}$ and $T = 1.0$: (a) normalized coherent intermediate scattering function $S(q, t)/S(q)$ from simulation. (b) $S(q, t)/S(q)$ predicted by the classical hydrodynamic theory, (c) incoherent intermediate scattering function $S_{inc}(q, t)$ from simulation, and (d) $S(q, t)/S(q)$ given by the convolution approximation.

The normalized coherent intermediate scattering functions from the simulations and hydrodynamic theory are given in Figs. 5(a) and 5(b), respectively. The de Gennes narrowing occurs around $q_{max} \approx 7.09 \, \sigma^{-1}$. Similar to the case of the coarse-grained polymer melt, the classical hydrodynamic theory does a reasonable job describing the major decay of the intermediate scattering function on the mesoscale at short correlation times. Interestingly, as we have already observed in the CG polymer melt, the "second ridge" of the hydrodynamic modes appears as a series of localized peaks in the simulation—a feature that is not captured by the continuum theory. It remains to be seen whether this phenomenon can be explained by any other existing theories. The incoherent scattering function is shown in Fig. 5(c). Since the liquid is not in a supercooled state, the ballistic regime is followed immediately by the normal diffusive behavior, i.e., $S_{inc}(q, t) \approx \exp(-Dq^2t)$, with a characteristic slope of $-1/2$. Figure 5(d) presents the intermediate scattering function predicted by the convolution approximation. In the mesoscopic regime, the theoretical contour lines of $S(q, t)/S(q)$ exhibit a characteristic slope of $-1/2$ [Fig. 5(d)], which is at odds with the true behavior from simulation [Fig. 5(a)].

It is helpful to point out that the mesoscopic collective dynamics of the CG polymer melt and LJ liquid are qualitatively similar [Figs. 2(a) and 5(a)]. On the other hand, their self-dynamics are drastically different in this regime: subdiffusive Rouse dynamics dominates the CG polymer melt (with a characteristic slope of $-1/4$), whereas the Lennard-Jones liquid displays free diffusion (with a slope of $-1/2$). Therefore, it is unlikely that one can treat both polymeric and nonpolymeric systems using the same model that employs the convolution approximation [61]. A comparison of the simulation data and the prediction of Eq. (11) is presented in Fig. 6. Similar to the results of the CG polymer system, the model of Novikov *et al.* fails to capture the qualitative features of the coherent intermediate scattering function in the mesoscopic regime.

C. NaCl and PEO melts

In this section we move beyond coarse-grained models and present results on more realistic and complicated systems, molten sodium chloride and poly(ethylene oxide). In these all-atom molecular dynamics simulations, we explore the wave number down to $q \approx 0.1 \, \text{Å}^{-1}$, which is considered the

mesoscale region in experiments. As we have emphasized in the preceding discussions, whether hydrodynamic modes play a role in a specific spatiotemporal regime generally should not be a matter of speculation, but should instead be settled by computation.

Figure 7(a) shows several spatiotemporal maps of the NaCl melt, including the normalized coherent intermediate scattering function $S(q, t)/S(q)$ from simulation, the $S(q, t)/S(q)$ predicted by the hydrodynamic theory, the normalized incoherent intermediate scattering function $S_{inc}(q, t)/S_{inc}(q)$ from simulation, and the $S(q, t)/S(q)$ predicted by the convolution approximation. A small de Gennes narrowing "peak" is observed near $q_{max} \approx 1.744 \, \text{Å}^{-1}$, in the $S(q, t)/S(q)$ 2D map from simulation. At the simulation temperature of $T = 1480$ K, the NaCl is not too far away from its melting point of $T_m \approx 1074$ K. Unlike the van der Waals interaction dominated systems in this investigation, the collective density fluctuations around the first structural peak in NaCl are not well separated from the modes on the mesoscopic scale. Whether this is a direct consequence of the long-range Coulombic interactions is not immediately apparent. What is clear, however, is that the spatiotemporal mapping method is effective in capturing such global features and raising new questions for future studies. Examining the slope of the contour lines of $S(q, t)/S(q)$, we find a scaling of -1 near $q \approx 0.1 \, \text{Å}^{-1}$, which is qualitatively consistent with the location of the hydrodynamic modes predicted by the classical theory. Nevertheless,
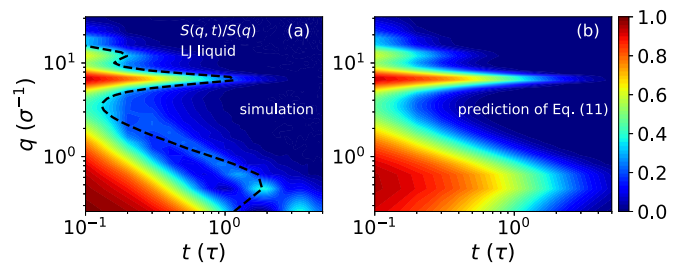

FIG. 6. Spatiotemporal mapping of the LJ liquid. Comparison between (a) the normalized coherent intermediate scattering function $S(q, t)/S(q)$ from simulation and (b) that obtained from Eq. (11). The theoretical $S(q, t)/S(q)$ is computed as $S(q, t)/S(q) = \exp[-t/\tau(q)]$. The black dashed line in (a) indicates the relaxation time $\tau(q)$ given by Eq. (11).
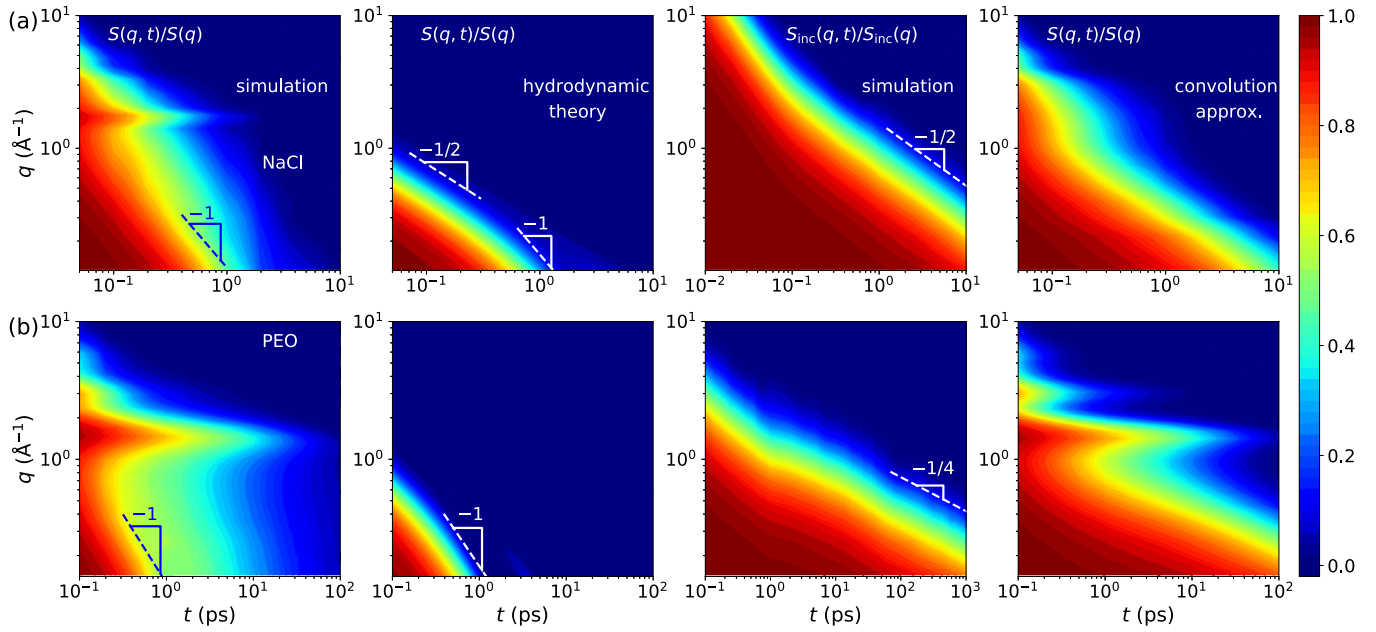
FIG. 7. Spatiotemporal mapping of the intermediate scattering functions of (a) NaCl and (b) PEO melt. The $S(q,t)/S(q)$ 2D maps obtained from simulation and hydrodynamic theory, the $S_{inc}(q,t)$ 2D map, and $S(q,t)/S(q)$ 2D map estimated by the convolution approximation are generated for each system. In the test of the convolution approximation, the systems are treated as monoatomic in order to yield a more self-consistent comparison.

in contrast to the cases of the coarse-grained polymer and LJ liquid, the theory does not work nearly as well here, failing to describe the decay of $S(q,t)/S(q)$ at long correlation times. Interestingly, while the normalized coherent intermediate scattering function of NaCl looks considerably different from that of the LJ liquid, their incoherent scattering functions are similar [Figs. 5(c) and 7(a)]. Lastly, the convolution approximation breaks down completely for NaCl, even around the first structural peak, i.e., the de Gennes narrowing region.

Figure 7(b) presents the results for the PEO melt. Once again, the classical hydrodynamic theory is able to capture the initial decay of the normalized coherent intermediate scattering function $S(q,t)/S(q)$ in the mesoscopic region. However, the simulation data exhibit a long tail that persists till tens of picoseconds. This feature is missed entirely by the theory. Note that the discrepancy between theory and simulation is much smaller in the case of the coarse-grained polymer melt. A major difference between the coarse-grained and atomistic models is that the PEO model includes a torsional potential in the intrachain interaction. Nevertheless, it is unclear if the long tail in the coherent intermediate scattering function should be attributed to the presence of the torsional potential. We note that a long tail is also observed in the NaCl simulation. More likely, the explanation lies in the multiatomic nature of the NaCl and PEO simulations. What we can conclude is that the mesoscopic collective dynamics in the examined spatiotemporal regime should involve both hydrodynamics and molecular physics. The incoherent scattering function $S_{inc}(q,t)/S_{inc}(q)$ of PEO is characterized by a slope of $-1/4$ on the 2D map around $q \approx 0.5$ Å^{-1} and $t \approx 10^3$ ps, indicating the Rouse dynamics of the polymer chain. Finally, the convolution approximation does not work

in the mesoscopic regime, which should not be surprising in light of the results for all the other systems.

To further evaluate Eq. (12), we compare the q-dependent relaxation time $\tau(q)$ from the PEO simulation with that predicted by Eq. (12) in Fig. 8. For simplicity, the $\tau(q)$ from the simulation is estimated as the correlation time at which $S(q,t)/S(q) = \exp(-1)$. On the other hand, we follow the same procedure that we have described for the CG polymer system to determine the fit parameters. Equation (12) gives a reasonable description of $\tau(q)$ at the first structural peak, but fails to produce the correct results in both the high- and low-q regions.
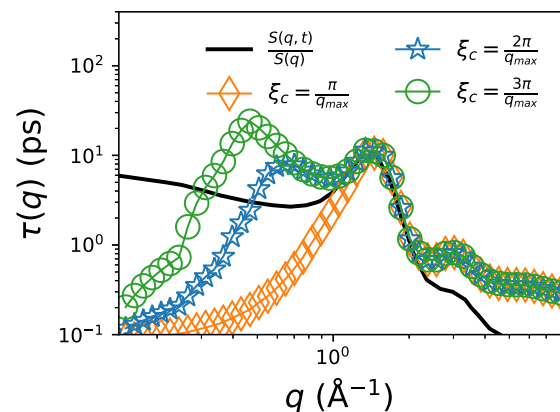

FIG. 8. Comparison of the q-dependent relaxation time $\tau(q)$ from the PEO simulation and the prediction by Eq. (12). Solid line: Simulation result based on $S(q,t)/S(q)$. Symbols: Predictions by Eq. (12) with different values of ξ_c.

IV. CONCLUDING REMARKS AND SUMMARY

From a mathematical point of view, space-time correlation functions are mappings defined on a four-dimensional space $[(\mathbf{r}, t)$ or $(\mathbf{q}, t)]$, and should be treated as such. For isotropic liquids at equilibrium, angular dependence vanishes, and one is concerned with the dynamic landscape on a two-dimensional plane $[(r, t)$ or $(q, t)]$. In other words, the spatiotemporal mapping method described in this work in fact is a natural way to think of the intermediate scattering functions as well as other space-time correlation functions in liquids. However, this is far from a prevailing practice in the field of liquid dynamics research. On the contrary, for historical reasons, the existing paradigm predicates on examining one-dimensional slices of these functions.

In this work we systematically demonstrate the benefits of adopting the spatiotemporal mapping approach by focusing on mesoscopic liquid dynamics. Our goal is not to resolve the complex origin of mesoscopic collective and self-dynamics in a single strike. Instead, we try to paint a broad picture about the usefulness of this different way of investigating liquid dynamics. Using a Lennard-Jones liquid, a coarse-grained bead-spring model, a molten sodium chloride, and a poly(ethylene oxide) as examples, we show that spatiotemporal maps of intermediate scattering functions provide a forum in which theories and simulations as well as inelastic scattering experiments can be conveniently explored. Specifically, we illustrate how different types of molecular motions can be identified by analyzing the slope of contour lines on two-dimensional maps. In addition, many subtle dynamical features that otherwise would be missed in the traditional one-dimensional analysis, can be easily revealed by the spatiotemporal mapping method. Most importantly, by surveying the global characteristics of these 2D maps, many new questions now can be asked. For example, how to explain the apparent difference between the coherent intermediate scattering functions of the coarse-grained and atomistic models in the mesoscopic regime? What is the origin of the localized hydrodynamic modes observed in the coarse-grained models? Is the overall enhanced correlation in collective dynamics of the coarse-grained polymer melt with decrease of temperature a signature of increasing molecular cooperativity? None of these questions could have been raised without the lens of the spatiotemporal mapping approach. As we have previously stated, it is not the intention of this work to give definitive answers to these questions. Addressing them requires careful experimental, computational, and theoretical investigations, which is beyond the scope of the present study. Lastly, while this work deals with density space-time correlation functions, the same spatiotemporal mapping method can be straightforwardly applied to other correlation functions.

TABLE III. Partial atomic charges.

Atom	q (e)
Methyl carbon (C)	0.09
Methylene carbon (C)	0.21225
Methyl hydrogen (H)	0.04375
Methylene hydrogen (H)	0.00450
Oxygen (O)	-0.4425

At this point we return to a question that we have intentionally avoided so far: what is mesoscale anyway? In some of the previous discussions on this topic [61,72,73], mesoscales are considered as length scales above intermolecular distances and below the long wavelength hydrodynamic limit. Our current study has revealed, however, *hydrodynamiclike* modes contribute substantially to the dynamics immediately beyond the first structural peak, in all the four simulated liquid systems. In light of this finding, we instead define mesoscale as a spatiotemporal regime beyond intermolecular distances, where liquid dynamics is still influenced by local molecular structures.

Finally, we mention some caveats regarding application of the 2D analysis approach to neutron spin-echo (NSE) experiments. It is well known that the normalized intermediate scattering function $S_{\text{NSE}}(q, t)$ from a typical NSE experiment contains contributions from both coherent and incoherent scattering processes:

$$S_{\text{NSE}}(q, t) = \frac{I_{\text{coh}}(q, t) - \frac{1}{3}I_{\text{inc}}(q, t)}{I_{\text{coh}}(q, 0) - \frac{1}{3}I_{\text{inc}}(q, 0)}, \qquad (13)$$

where $I_{\text{coh}}(q, t)$ and $I_{\text{inc}}(q, t)$ are coherent and incoherent intensities, respectively. In certain systems such as CKN [5], incoherent contributions are negligibly small and $S_{\text{NSE}}(q, t)$ is dominated by coherent dynamics. For some polymeric materials such as polyisobutylene [6], it is possible to determine the coherent normalized intermediate scattering function $S(q, t)/S(q)$, by polarization analysis and measurement of a fully hydrogenous sample. In general, however, coherent and incoherent contributions may not be easily separated by NSE in the mesoscopic regime. Nevertheless, even in this case, data analysis can still potentially benefit from a 2D analysis approach, as coherent and incoherent dynamics exhibit rather different spatiotemporal characteristics on mesoscopic scales. Lastly, we note that there are limitations on the spatial and temporal regimes that can be accessed by the NSE technique. In particular, correlation times shorter than $\sim$1 ps cannot be easily probed, making it difficult to fully resolve hydrodynamiclike responses in many systems.

TABLE II. Lennard-Jones potential coefficients.

Atom	ϵ (kcal/mol)	σ (Å)
C	0.1078	3.3977
H	0.0208	2.4220
O	0.0726	3.1561

TABLE IV. Harmonic potential coefficients.

Bond	k_{ij}^s (kcal/mol Å^{-2})	r_{ij}^0 (Å)
C-C	232.52	1.5215
C-H	375.92	1.1025
C-O	284.76	1.4134

APPENDIX: FORCE FIELD FOR POLY(ETHYLENE OXIDE)

Our atomistic model of poly(ethylene oxide) (PEO) melt is based on the General Amber Force Field (GAFF) [46]. The interaction energy between atoms is expressed by the sum of both nonbonded and bonded potentials as

$$E = \sum_{\substack{\text{nonbonded} \\ \text{pairs}}} E^{\text{NB}}(r_{ij}) + \sum_{\text{bonds}} E^s(r_{ij}) + \sum_{\text{angles}} E^b(\theta_{ijk}) \\ + \sum_{\text{torsions}} E^t(\phi_{ijkl}), \tag{A1}$$

where r_{ij} is the separation between atoms i and j, $E^{\text{NB}}(r_{ij})$ and $E^s(r_{ij})$ are the nonbonded and bonded pairwise potentials, respectively, $E^b(\theta_{ijk})$ is the angular potential due to bending of the valence angle between atoms i, j, and k, and $E^t(\phi_{ijkl})$ is the torsional potential associated with twisting of the dihedral angle defined by atoms i, j, k, and l. The force field parameters were optimized by comparing molecular dynamics (MD) simulation results with density functional theory (DFT) calculations, as stated in the main text. The optimized parameters are detailed below.

The nonbonded interaction in GAFF is given by

$$E^{\text{NB}}(r_{ij}) = 4\epsilon \left[\left(\frac{\sigma}{r_{ij}} \right)^{12} - \left(\frac{\sigma}{r_{ij}} \right)^6 \right] + \frac{C q_i q_j}{r_{ij}}, \tag{A2}$$

where the constant C is 332.0636 kcal Å/(mol e^2). In our simulations, the values of ϵ and σ were directly adapted from GAFF without any further modification (Table II) [46]. As is the convention, the Lorentz-Berthelot combining rules were used for pair coefficients for atoms of different types. The Lennard-Jones interaction was truncated at 10 Å. The atomic

TABLE V. Angular potential coefficients.

Angle	k_{ijk}^b (kcal/mol)	θ_{ijk}^0 (deg)
C-C-H	46.868	109.6844
C-C-O	85.306	107.6154
C-O-C	66.293	112.7511
H-C-H	38.802	107.4976
H-C-O	62.377	111.1791

point charges were obtained from *ab initio* calculations using the restrained electrostatic potential (RESP) method [79,80] with the ANTECHAMBER software [81]. The charges were further adjusted to ensure electrical neutrality of the PEO chain, regardless of the degree of polymerization. The final charges for each type of atom are listed in Table III. The harmonic potentials for the covalent bonds are of the form

$$E^s(r_{ij}) = k_{ij}^s \left(r_{ij} - r_{ij}^0 \right)^2, \tag{A3}$$

where the force constant k_{ij}^s is directly adopted from GAFF, and the equilibrium atomic distance r_{ij}^0 is based on the *ab initio* calculations. The values of k_{ij}^s and r_{ij}^0 for each bond type are shown in Table IV. The potential energy due to bending of the covalent bond is expressed as

$$E^b(\theta_{ijk}) = k_{ijk}^b \left(\theta_{ijk} - \theta_{ijk}^0 \right)^2. \tag{A4}$$

Similarly, the bending force constant k_{ijk}^b is taken from GAFF, and the equilibrium valence angle θ_{ijk}^0 is from the *ab initio* structure. The values of k_{ijk}^b and θ_{ijk}^0 for each bond type are given in Table V. Lastly, the dihedral terms are described by

$$E^t(\phi_{ijkl}) = \sum_n k_{ijkl}^t \left[1 + \cos(n\phi_{ijkl} - \phi_{ijkl}^0) \right], \tag{A5}$$

where ϕ_{ijkl} is the dihedral angle formed by the four atoms i, j, k, and l in sequence, k_{ijkl}^t is the torsional force constant, n is multiplicity, and ϕ_{ijkl}^0 is the phase angle. The parameters for these torsional potentials are shown in Table VI. Following the conventions used for Amber-type force fields, the intramolecular nonbonded interactions between atoms separated by one or two bonds ("1-2" and "1-3" interactions) were set to zero in the simulations. Additionally, the Lennard-Jones and electrostatic pairwise interactions between atoms separated by three bonds ("1-4" interactions) are scaled by 0.5 and 0.8333, respectively. The interactions for atom pairs separated by more than three bonds were unscaled.

TABLE VI. Dihedral potential coefficients.

Dihedral angle	Multiplicity	ϕ_{ijkl}^0 (deg)	k_{ijkl}^t (kcal/mol)
C-C-O-C	1	0	0.0675
C-C-O-C	2	0	0.0625
C-C-O-C	3	0	0.2500
H-C-C-H	3	0	0.1556
H-C-C-O	1	0	0.2500
H-C-C-O	3	0	0.1375
H-C-O-C	3	0	0.3370
O-C-C-O	1	180	0.6520
O-C-C-O	2	0	0.3094
O-C-C-O	3	0	0.1375

[1] P. Egelstaff, *An Introduction to the Liquid State* (Academic, New York, 1967).

[2] J.-P. Hansen and I. R. McDonald, *Theory of Simple Liquids: With Applications to Soft Matter* (Academic, New York, 2013).

[3] M. P. Allen and D. J. Tildesley, *Computer Simulation of Liquids*, 2nd ed. (Oxford University Press, Oxford, 2017).

[4] J. P. Boon and S. Yip, *Molecular Hydrodynamics* (Courier Corporation, North Chelmsford, MA, 1991).

[5] F. Mezei, W. Knaak, and B. Farago, Neutron spin echo study of dynamic correlations near liquid-glass transition, Phys. Scr. **T19B**, 363 (1987).

[6] B. Farago, A. Arbe, J. Colmenero, R. Faust, U. Buchenau, and D. Richter, Intermediate length scale dynamics of polyisobutylene, Phys. Rev. E **65**, 051803 (2002).

[7] A. Faraone, K. Hong, L. R. Kneller, M. Ohl, and J. R. D. Copley, Coherent dynamics of meta-toluidine investigated by quasielastic neutron scattering, J. Chem. Phys. **136**, 104502 (2012).

[8] W. Chen, S. Watson, Y. Qiu, J. A. Rodriguez-Rivera, and A. Faraone, Wide-angle polarization analysis on the multi-axis crystal spectrometer for the study of collective and single particle dynamics of methanol at its prepeak, Physica B **564**, 166 (2019).

[9] A. Arbe, G. J. Nilsen, J. R. Stewart, F. Alvarez, V. G. Sakai, and J. Colmenero, Coherent structural relaxation of water from meso- to intermolecular scales measured using neutron spectroscopy with polarization analysis, Phys. Rev. Research **2**, 022015(R) (2020).

[10] I. M. Mryglod, I. P. Omelyan, and M. V. Tokarchuk, Generalized collective modes for the Lennard-Jones fluid, Mol. Phys. **84**, 235 (1995).

[11] M. Tarek and D. J. Tobias, Single-Particle and Collective Dynamics of Protein Hydration Water: A Molecular Dynamics Study, Phys. Rev. Lett. **89**, 275501 (2002).

[12] N. Anento, J. A. Padró, O. Alcaraz, and J. Trullàs, Molecular dynamics simulation of collective motions in binary liquids, Mol. Simul. **29**, 373 (2003).

[13] Y. Khairy, F. Alvarez, A. Arbe, and J. Colmenero, Collective features in polyisobutylene. A study of the static and dynamic structure factor by molecular dynamics simulations, Macromolecules **47**, 447 (2014).

[14] E. J. Haddadian, H. Zhang, K. F. Freed, and J. F. Douglas, Comparative study of the collective dynamics of proteins and inorganic nanoparticles, Sci. Rep. **7**, 41671 (2017).

[15] T. Bryk and J.-F. Wax, Collective dynamics in a liquid polyvalent metal: Liquid thallium at the melting point, J. Chem. Phys. **132**, 074504 (2010).

[16] S. Bellissima, S. de Panfilis, U. Bafile, A. Cunsolo, M. A. González, E. Guarini, and F. Formisano, The hydrogen-bond collective dynamics in liquid methanol, Sci. Rep. **6**, 1 (2016).

[17] A. Widmer-Cooper and P. Harrowell, On the study of collective dynamics in supercooled liquids through the statistics of the iso-configurational ensemble, J. Chem. Phys. **126**, 154503 (2007).

[18] Wide angle spin-echo spectrometer at ILL: https://www.ill.eu/users/instruments/instruments-list/wasp/description/instrument-layout.

[19] S. Plimpton, Fast parallel algorithms for short-range molecular dynamics, J. Comput. Phys. **117**, 1 (1995).

[20] W. M. Brown, P. Wang, S. J. Plimpton, and A. N. Tharrington, Implementing molecular dynamics on hybrid high performance computers–short range forces, Comput. Phys. Commun. **182**, 898 (2011).

[21] LAMMPS website: http://lammps.sandia.gov.

[22] D. Levesque and L. Verlet, Molecular dynamics calculations of transport coefficients, Mol. Phys. **61**, 143 (1987).

[23] D. Levesque, L. Verlet, and J. Kürkijarvi, Computer 'experiments' on classical fluids. IV. transport properties and time-correlation functions of the Lennard-Jones liquid near its triple point, Phys. Rev. A **7**, 1690 (1973).

[24] I. M. de Schepper, E. G. D. Cohen, C. Bruin, J. C. van Rijs, W. Montfrooij, and L. A. de Graaf, Hydrodynamic time correlation functions for a Lennard-Jones fluid, Phys. Rev. A **38**, 271 (1988).

[25] L. Verlet and J.-J. Weis, Equilibrium theory of simple liquids, Phys. Rev. A **5**, 939 (1972).

[26] S.-H. Chen and A. Rahman, Molecular dynamics simulation of dense gases: I. Test particle motion, Mol. Phys. **34**, 1247 (1977).

[27] A. Rahman, Correlations in the motion of atoms in liquid argon, Phys. Rev. **136**, A405 (1964).

[28] A. Rahman, Current fluctuations in classical liquids, in *Proceedings of a Symposia on Neutron Inelastic Scattering* (International Atomic Energy Agency, Copenhagen, 1968), pp. 561–572.

[29] L. Verlet, Computer 'experiments' on classical fluids. II. Equilibrium correlation functions, Phys. Rev. **165**, 201 (1968).

[30] J. W. E. Lewis and S. W. Lovesey, Short-wavelength collective density excitations in monatomic liquids, J Phys C: Solid State Phys **10**, 3221 (1977).

[31] N. K. Ailawadi, B. J. Berne, and D. Forster, Light scattering from shear waves: The role of angular momentum fluctuations in light scattering, Phys. Rev. A **3**, 1472 (1971).

[32] I. M. de Schepper, J. C. van Rijs, A. A. van Well, P. Verkerk, L. A. de Graaf, and C. Bruin, Microscopic sound waves in dense Lennard-Jones fluids, Phys. Rev. A **29**, 1602 (1984).

[33] E. Enciso, N. G. Almarza, V. del Prado, F. J. Bermejo, E. López Zapata, and M. Ujaldón, Molecular-dynamics simulation on simple fluids: Departure from linearized hydrodynamic behavior of the dynamical structure factor, Phys. Rev. E **50**, 1336 (1994).

[34] M. Schoen, R. Vogelsang, and C. Hoheisel, Computation and analysis of the dynamic structure factor $S(k, \omega)$ for small wave vectors: A molecular dynamics study for a Lennard-Jones liquid, Mol. Phys. **57**, 445 (1986).

[35] J.-P. Hansen and L. Verlet, Phase transitions of the Lennard-Jones system, Phys. Rev. **184**, 151 (1969).

[36] D. Frenkel and B. Smit, *Understanding Molecular Simulation: From Algorithms to Applications*, 2nd ed. (Elsevier, Amsterdam, 2001).

[37] B. Smit, Phase diagrams of Lennard-Jones fluids, J. Chem. Phys. **96**, 8639 (1992).

[38] K. Kremer and G. S. Grest, Dynamics of entangled linear polymer melts: A molecular-dynamics simulation, J. Chem. Phys. **92**, 5057 (1990).

[39] G. S. Grest, Communication: Polymer entanglement dynamics: Role of attractive interactions, J. Chem. Phys. **145**, 141101 (2016).

[40] H.-P. Hsu and K. Kremer, Static and dynamic properties of large polymer melts in equilibrium, J. Chem. Phys. **144**, 154907 (2016).

[41] J. D. Weeks, D. Chandler, and H. C. Andersen, Role of repulsive forces in determining the equilibrium structure of simple liquids, J. Chem. Phys. **54**, 5237 (1971).

[42] D. J. Adams and I. R. McDonald, Rigid-ion models of the interionic potential in the alkali halides, J Phys C: Solid State Phys **7**, 2761 (1974).

[43] F. G. Fumi and M. P. Tosi, Ionic sizes and born repulsive parameters in the NaCl-type alkali halides—I: The Huggins-Mayer and Pauling forms, J. Phys. Chem. Solids. **25**, 31 (1964).

[44] M. P. Tosi and F. G. Fumi, Ionic sizes and born repulsive parameters in the NaCl-type alkali halides—II: The generalized Huggins-Mayer form, J. Phys. Chem. Solids. **25**, 45 (1964).

[45] R. W. Hockney and J. W. Eastwood, *Computer Simulation Using Particles* (Taylor & Francis Group, New York, 1988).

[46] J. Wang, R. M. Wolf, J. W. Caldwell, P. A. Kollman, and D. A. Case, Development and testing of a general amber force field, J. Comput. Chem. **25**, 1157 (2004).

[47] H. Yoshida and H. Matsuura, Density functional study of the conformations and vibrations of 1,2-dimethoxyethane, J. Phys. Chem. A **102**, 2691 (1998).

[48] M. Valiev, E. J. Bylaska, N. Govind, K. Kowalski, T. P. Straatsma, H. J. J. van Dam, D. Wang, J. Nieplocha, E. Apra, and T. L. Windus, NWCHEM: A comprehensive and scalable open-source solution for large scale molecular simulations, Comput. Phys. Commun. **181**, 1477 (2010).

[49] V. F. Sears, Neutron scattering lengths and cross sections, Neutron News **3**, 26 (1992).

[50] Neutron scattering lengths and cross sections: https://www.ncnr.nist.gov/resources/n-lengths/.

[51] OpenACC website: http://openacc.org.

[52] B. J. Berne and R. Pecora, *Dynamic Light Scattering: With Applications to Chemistry, Biology, and Physics* (Dover, New York, 2000).

[53] E. Sheldon and D. M. van Patter, Compound inelastic nucleon and gamma-ray angular distributions for even-and odd-mass nuclei, Rev. Mod. Phys. **38**, 143 (1966).

[54] R. D. Mountain, Thermal relaxation and Brillouin scattering in liquids, J. Res. Natl. Bur. Stand. A Phys. Chem. **70A**, 207 (1966).

[55] M. S. Green, Markoff random processes and the statistical mechanics of time-dependent phenomena. II. Irreversible processes in fluids, J. Chem. Phys. **22**, 398 (1954).

[56] R. Kubo, Statistical-mechanical theory of irreversible processes. I. General theory and simple applications to magnetic and conduction problems, J. Phys. Soc. Jpn. **12**, 570 (1957).

[57] P. G. de Gennes, Liquid dynamics and inelastic scattering of neutrons, Physica **25**, 825 (1959).

[58] K. Sköld, Small Energy Transfer Scattering of Cold Neutrons from Liquid Argon, Phys. Rev. Lett. **19**, 1023 (1967).

[59] K. Sköld and K. E. Larsson, Atomic motion in liquid argon, Phys. Rev. **161**, 102 (1967).

[60] G. H. Vineyard, Scattering of slow neutrons by a liquid, Phys. Rev. **110**, 999 (1958).

[61] V. N. Novikov, K. S. Schweizer, and A. P. Sokolov, Coherent neutron scattering and collective dynamics on mesoscale, J. Chem. Phys. **138**, 164508 (2013).

[62] W.-S. Xu, J. F. Douglas, and K. F. Freed, Influence of cohesive energy on the thermodynamic properties of a model glass-forming polymer melt, Macromolecules **49**, 8341 (2016).

[63] Origins of Jet Color maps: https://blogs.mathworks.com/cleve/2015/02/02/origins-of-colormaps/.

[64] B. Frick and D. Richter, The microscopic basis of the glass transition in polymers from neutron scattering studies, Science **267**, 1939 (1995).

[65] P. Falus, M. A. Borthwick, S. Narayanan, A. R. Sandy, and S. G. J. Mochrie, Crossover from Stretched to Compressed Exponential Relaxations in a Polymer-Based Sponge Phase, Phys. Rev. Lett. **97**, 066102 (2006).

[66] L. Hong, N. Smolin, and J. C. Smith, de Gennes Narrowing Describes the Relative Motion of Protein Domains, Phys. Rev. Lett. **112**, 158102 (2014).

[67] Z. Wang, C. E. Bertrand, W.-S. Chiang, E. Fratini, P. Baglioni, A. Alatas, E. E. Alp, and S.-H. Chen, Inelastic x-ray scattering studies of the short-time collective vibrational motions in hydrated lysozyme powders and their possible relation to enzymatic function, J. Phys. Chem. B **117**, 1186 (2013).

[68] P.-G. de Gennes, Quasi-elastic scattering of neutrons by dilute polymer solutions: I. Free-draining limit, Phys. Phys. Fiz. **3**, 37 (1967).

[69] D. Richter, B. Ewen, B. Farago, and T. Wagner, Microscopic Dynamics and Topological Constraints in Polymer Melts: A Neutron-Spin-Echo Study, Phys. Rev. Lett. **62**, 2140 (1989).

[70] W. Kob and H. C. Andersen, Testing mode-coupling theory for a supercooled binary Lennard-Jones mixture I: The van Hove correlation function, Phys. Rev. E **51**, 4626 (1995).

[71] F. Sciortino, P. Gallo, P. Tartaglia, and S.-H. Chen, Supercooled water and the kinetic glass transition, Phys. Rev. E **54**, 6331 (1996).

[72] J. Colmenero, F. Alvarez, Y. Khairy, and A. Arbe, Modeling the collective relaxation time of glass-forming polymers at intermediate length scales: Application to polyisobutylene, J. Chem. Phys. **139**, 044906 (2013).

[73] J. Colmenero, F. Alvarez, and A. Arbe, Collective dynamics of glass-forming polymers at intermediate length scales—A synergetic combination of neutron scattering, atomistic simulations and theoretical modelling, in *EPJ Web Conference*, Vol. 83 (EDP Sciences, France, 2015), p. 01001.

[74] K. S. Singwi and A. Sjölander, Resonance absorption of nuclear gamma rays and the dynamics of atomic motions, Phys. Rev. **120**, 1093 (1960).

[75] A. Arbe, J. Rubio, P. Malo de Molina, J. Maiz, J. A. Pomposo, P. Fouquet, S. Prevost, F. Juranyi, M. Khaneft, and J. Colmenero, Melts of single-chain nanoparticles: A neutron scattering investigation, J. Appl. Phys. **127**, 044305 (2020).

[76] E. Kartini, M. F. Collins, B. Collier, F. Mezei, and E. C. Svensson, Inelastic-neutron-scattering studies on glassy and liquid $Ca_{0.4}K_{0.6}(NO_3)_{1.4}$, Phys. Rev. B **54**, 6292 (1996).

[77] C. Tengroth, J. Swenson, and L. Börjesson, A neutron diffraction study of $Ca_{0.4}K_{0.6}(NO_3)_{1.4}$ from the glass to liquid state, Physica B **234-236**, 414 (1997).

[78] M. C. C. Ribeiro, First sharp diffraction peak in the fragile liquid $Ca_{0.4}K_{0.6}(NO_3)_{1.4}$, Phys. Rev. B **61**, 3297 (2000).

[79] C. I. Bayly, P. Cieplak, W. Cornell, and P. A. Kollman, A well-behaved electrostatic potential based method using charge restraints for deriving atomic charges: The RESP model, J. Phys. Chem. **97**, 10269 (1993).

[80] P. Cieplak, W. D. Cornell, C. Bayly, and P. A. Kollman, Application of the multimolecule and multiconformational RESP methodology to biopolymers: Charge derivation for DNA, RNA, and proteins, J. Comput. Chem. **16**, 1357 (1995).

[81] Website for the Antechamber software: http://ambermd.org/ antechamber/.